

The dynamics and electromagnetic signatures of accretion in unequal mass binary black hole inspirals

Madeline Clyburn¹^{*} & Jonathan Zrake¹[†]

¹*Department of Physics and Astronomy, Clemson University, Clemson, SC 29634, USA*

Accepted XXX. Received YYY; in original form ZZZ

ABSTRACT

We present a theoretical study of the gravitational wave (GW) driven inspirals of accreting black hole binaries with mass $M = 10^7 M_{\odot}$ and mass ratios between 10^{-3} and 10^{-1} . Our results are based on analytic estimates, and grid-based hydrodynamics simulations run for many thousands of binary orbits before the merger. We show that the GW inspiral is evident in the light curves and color evolution of a binary-hosting quasar, over years to decades before a merger. The long-term electromagnetic (EM) signature is characterized by a gradual UV brightening, and X-ray dimming, followed by an X-ray disappearance hours to days before the GW burst, and finally a years-like re-brightening as the disk relaxes and refuels the remnant black hole. These timescales are surprisingly insensitive to the amplitude of viscous stress in the disk. The spectrum of quasi-thermal disk emission shows two peaks: one in the UV, and another in the X-ray, associated with the outer and circum-secondary disks respectively; emission from the inner disk is suppressed because the secondary consumes most of the inflowing gas. We discuss implications for real-time and archival EM followup of GW bursts detected by *LISA*.

Key words: accretion disks – black hole physics – black hole mergers – hydrodynamics

1 INTRODUCTION

The gravitational wave (GW) driven inspirals of massive black hole binaries (MBHB’s) are high priority targets for the future space-based GW detector *LISA* (Amaro-Seoane et al. 2023). *LISA* will observe the GW’s emitted by MBHB’s in the final hours to months of their lives (e.g. Sesana 2021), including the GW burst produced as they merge, and the ring-down of the final black hole remnant (Baibhav et al. 2020; Pitte et al. 2023). These observations will directly constrain the binary component masses and spins (e.g. Trias & Sintes 2008), and could reveal the presence of a circumbinary gas disk (Yunes et al. 2011; Derdzinski et al. 2019, 2021; Garg et al. 2024).

The science potential of a *LISA* detection is greatly increased if the host galaxy can be identified. The host morphology could reveal evidence of recent galaxy mergers (e.g. Hughes 2002; Izquierdo-Villalba et al. 2022), potentially constraining the timescale for MBHB formation (Begelman et al. 1980). Also the host redshift, combined with the GW luminosity distance, yields a measurement of the Hubble constant (Schutz 1986). However, *LISA* observations of MBHB inspirals will have angular resolutions on the order of $1 - 10 \text{ deg}^2$, generally too poor to identify the host galaxies of individual events (Mangiagli et al. 2020). It is therefore of considerable interest to examine the prospects to identify electromagnetic (EM) counterparts to GW observations of MBHB inspirals.

The MBHB’s that will merge as *LISA* sources likely exist in the gas-rich nuclear regions of post-merger galaxies (Barnes & Hernquist 1996), and could thus be surrounded by an optically thick accretion

flow. The flow would consist of an outer (circumbinary) disk, an inner disk around the primary (more massive) black hole, and a smaller “minidisk” around the secondary (less massive) black hole. The quasi-thermal radiation released from the accretion flow could exhibit distinctive temporal or spectral characteristics, which may aid in the identification of a host galaxy, either in archival data from time-domain EM surveys, or with contemporaneous tiling of the *LISA* error box.

Predicting such EM signatures requires a detailed understanding of how the accretion flow evolves in time throughout the binary inspiral, and many studies have now been carried out based on multi-dimensional (magneto-)hydrodynamics simulations (Farris et al. 2010, 2011, 2012; Noble et al. 2012; Farris et al. 2015; Tang et al. 2018; Bowen et al. 2018, 2019; Derdzinski et al. 2019; Pereira et al. 2019; Derdzinski et al. 2021; Combi et al. 2021; Gutiérrez et al. 2022; Ruiz et al. 2023; Avara et al. 2023; Dittmann et al. 2023; Krauth et al. 2023b; Cocchiararo et al. 2024; Franchini et al. 2024). Each of these is based on equal-mass binary inspirals, except for Ruiz et al. (2023), which includes a model with mass ratio as low as $q \equiv M_2/M_1 = 0.25$, and Pereira et al. (2019) and Derdzinski et al. (2019, 2021), which include intermediate mass-ratio inspirals (so-called IMRI’s; Arca Sedda et al. 2021), in the range of $q = 10^{-2}$ to 10^{-4} . The study led by Pereira reports the time-evolving mass accretion rates, but not EM signatures, and the studies led by Derdzinski analyze the magnitude of gas-induced deviations from the vacuum post-Newtonian inspiral, but also do not characterize the EM signatures. Very recently, Cocchiararo et al. (2024) reported EM signatures for mass ratios as small as $q = 0.1$.

In this paper, we use multi-dimensional hydrodynamics simulations to characterize the EM signatures of IMRI’s, with q in the range

^{*} E-mail: clyburn@clemson.edu

[†] E-mail: jzrake@clemson.edu

of 10^{-3} to 10^{-1} . Our interest in IMRI's is motivated by the possibility that a large fraction of the MBHB population could have significantly unequal masses (Sesana et al. 2012; Bellovary et al. 2019), and that IMRI's, if surrounded by gas, might produce “cleaner” EM signatures than systems with nearly equal component masses. Indeed, gas accretion in systems with $q \lesssim 0.04$ has been seen to operate in a different regime, characterized by much reduced stochastic variability (D’Orazio et al. 2016), and this could increase the significance of EM counterpart identifications based on periodic or long-term changes of appearance throughout the inspiral. IMRI's are also of particular interest because the lower-mass component black holes will be in the range of $10^3\text{--}5 M_\odot$, meaning that *LISA* observations of them would directly probe a population of intermediate mass black holes, which has so far been elusive (e.g. Miller 2009).

Accreting IMRI's might also present distinctive spectral signatures to distinguish them from MBHB's with nearly equal component masses. This is because the less massive black hole is generally expected to consume a majority of the inflowing gas (Lubow et al. 1999; Duffell et al. 2020; Muñoz et al. 2020), an effect referred to in literature as preferential accretion (e.g. Siwek et al. 2020, 2023a). The effect implies that emission from the secondary minidisk could dominate the system's overall EM luminosity, or that the spectral energy distribution of quasi-thermal disk emission could exhibit multiple peaks. Also, if the degree of preferential accretion changes throughout the late inspiral, that might imprint a distinctive color evolution that could be used to photometrically select host galaxy candidates from time-domain surveys. Thus, a main goal of this study is to measure the evolution of the component accretion rates \dot{M}_1 and \dot{M}_2 throughout a GW-driven inspiral, and use those measurements to approximate the color evolution of accreting IMRI's.

To the best of our knowledge, the present study is the first to use multi-dimensional hydrodynamics simulations to model the EM emission of accreting IMRI's. However, the earliest papers on EM emission from MBHB inspirals, which were based on one-dimensional disk models, focused specifically on systems with mass ratios $q \lesssim 0.1$. Armitage & Natarajan (2002) used the “cold disk” equations (e.g. Pringle 1981) to model how the inner and outer disks evolve throughout the inspiral. They used an empirical term derived from the theory of disk-satellite interactions (Goldreich & Tremaine 1980; Lin & Papaloizou 1986) to model the tidal torque applied to the disk by the secondary. Such treatments can lead to the formation of a vacuum gap surrounding the secondary's orbit, prohibiting mass from moving between the inner and outer disks, or onto the secondary black hole. As the GW inspiral speeds up, the vacuum gap implies “tidal squeezing” of the inner disk toward the primary black hole. Armitage & Natarajan (2002) speculated that this process (now sometimes referred to as a “snowplow” mechanism) force-feeds the larger black hole and could drive a massive outflow and EM flare in the very late inspiral. The studies of Lodato et al. (2009) and Chang et al. (2010) are similarly based on time-dependent one-dimensional disk models, and also support the possibility of a snowplow mechanism.

However, the vacuum gap around the secondary's orbit is now understood to be an artifact of one-dimensional disk treatments. Two-dimensional calculations show that gas crosses the secondary orbit on so-called “horseshoe” orbits (Lubow et al. 1999; Duffell et al. 2014; Fung et al. 2014). It means that the inner disk gas could be expelled to the outer disk, or consumed by the secondary, and that a late-inspiral enhancement of the accretion rate may not take place (Baruteau et al. 2012). In fact, the opposite effect has been seen in simulations of equal-mass binaries (e.g. Farris et al. 2015; Dittmann et al. 2023; Krauth et al. 2023b; Franchini et al. 2024); the binary

accretion rate drops throughout the late inspiral. We refer to such mass starvation as “viscous decoupling,” an effect first described in Liu et al. (2003). It happens because the binary eventually contracts faster than the inward viscous spreading of the outer disk, and this leads to a diminishing rate of mass supply to the binary components. It was also pointed out in Milosavljević & Phinney (2005) that viscous decoupling of the binary should lead to a post-merger re-brightening, as the disk spreads inwards following the merger, and eventually begins fueling the black hole remnant. The re-fueling has been simulated for the case of post-merger equal-mass binaries in Farris et al. (2015) and Krauth et al. (2023b), and we examine it in this study for the case of intermediate mass ratios $q < 0.1$.

Our study is based on time-dependant numerical solutions of the two-dimensional (vertically averaged) Navier-Stokes equations, where gas is subject to the time-dependant gravitational potential of an unequal-mass black hole binary, undergoing a GW-driven post-Newtonian inspiral (Peters 1964). We adopt a simplified thermodynamic treatment, in which the speed of sound is set to a small fraction, $1/\mathcal{M}$, of the local escape speed (\mathcal{M} is a global Mach number, selected to be in the range of 10 – 20). The bolometric EM luminosity is reasonably well predicted by measurements of the mass accretion rate, provided the flow is radiatively efficient. Owing to the use of simplified thermodynamic treatment, our simulations do not yield a self-consistent disk photosphere temperature. To model the color evolution, we have thus developed a “three-disk” toy model for the disk surface temperature, based on approximating the inner, outer, and secondary disks as stationary α -disks (Shakura & Sunyaev 1973), with simulation-calibrated mass inflow rates. We believe this approach yields a reasonable first approximation of the color evolution of accreting IMRI's. Models with self-consistent thermodynamics (e.g. Westernacher-Schneider et al. 2022, 2024) will be reported in a follow-up study.

Our paper is organized as follows. In Sec. 2 we describe the physical picture of the MBHB inspiral and provide analytical estimates for the EM emission from these systems. In Sec. 3 we describe the equations of motion, initial conditions, and the numerical setup. Sec. 4 contains the key dynamical measurements obtained from the numerical simulations. Sec. 5 includes the predictions of spectral evolution and light curves, based on the three-disk spectral toy model, and discusses prospects for EM detections of *LISA* sources. Finally, in Sec. 6 we summarize our results, discuss some caveats, and describe plans for future work.

2 ACCRETING UNEQUAL MASS BLACK HOLE BINARIES

2.1 Fiducial System

We adopt a fiducial black hole binary that will be detectable by *LISA* out to a high redshift. The total mass of the fiducial system is $M = 10^7 M_\odot$, the mass ratio is $q = 0.01$, and the orbit is circular. The assumption of a circular orbit is justified on the basis that in the late inspiral stage, the GW radiative back-reaction exceeds the gravitational forces of the gas, so the orbital eccentricity, driven up at wider binary separations (Zrake et al. 2021; D’Orazio & Duffell 2021; Siwek et al. 2023b), has already been dissipated. At the leading post-Newtonian order, the rate of orbital contraction due to GW's is given in Peters (1964) as

$$\dot{a}_{\text{gw}} = -\frac{64G^3 M^3 \eta}{5c^5 a^3}, \quad (1)$$

where $\eta \equiv q/(1+q)^2 = M_1 M_2 / M^2$ and a is the size of the orbit. If the fiducial binary were on track to merge in the next 50 years,

then it would presently have a semi-major axis $a_0 \simeq 6.3$ AU and an orbital period $P_0 \simeq 1.8$ days. The time-to-coalescence is denoted as $t_{\text{minus}} \equiv \tau/4$, where $\tau \equiv -a/\dot{a}_{\text{gw}}$ is the nominal orbital contraction timescale. The fiducial system is very mildly relativistic, with the orbital velocity roughly equivalent to $0.17c$, and gravitational radius $r_g \equiv GM/c^2$ about 64 times smaller than the initial semi-major axis. For later reference, the three (small) relativistic parameters v/c , r_g/a , and P/τ are mutually related via Eqn. 1,

$$\left(\frac{v}{c}\right)^2 = \frac{r_g}{a} = \left(\frac{5P}{128\pi\eta\tau}\right)^{2/5}. \quad (2)$$

The Eddington luminosity of a $10^7 M_\odot$ black hole is $L_{\text{edd}} \simeq 1.15 \times 10^{45}$ erg/s, corresponding to a bolometric absolute magnitude of $M_{\text{bol}} \simeq -24$. For reference, such modest-luminosity AGN will be detectable by *LSST* out to redshifts of $z \simeq 5.5$. (Brandt et al. 2009). The *LISA* detection horizon for these events will be at redshifts of $z \simeq 20$ (Sesana 2021).

2.2 Physical Picture and Spectral Appearance

The binary is surrounded by a thin, centrifugally supported, optically thick gas flow. In binaries with a small mass ratio, the overall flow is similar to that of planet-forming disks. It comprises an outer circumbinary disk, a low-density annular gap surrounding the secondary’s orbit, and an inner disk around the primary.

The accretion flow appears as a multi-temperature blackbody; the spectrum is determined by the distribution of the local disk photosphere temperatures. To get a sense for the composite spectrum of the accretion flow, including the outer disk, the inner disk, and the secondary minidisk, it is instructive to consider each of these disks as a steady state α -disk (Shakura & Sunyaev 1973), and examine the composite quasi-thermal emission spectrum. The characteristic temperatures are given by

$$\begin{aligned} T_{\text{outer}} &= (3GM\dot{M}/8\pi a^3\sigma)^{1/4} \\ T_i &= (3GM_i\dot{M}_i/8\pi R_i^3\sigma)^{1/4} \propto \dot{M}_i^{1/4} M_i^{-1/2} \end{aligned} \quad (3)$$

where $i = 1$ for the primary and $i = 2$ for the secondary, and $R_i = 6GM_i/c^2$ are the inner cutoff radii of the component disks. For the fiducial system discussed in Sec. 2.1, accreting at the Eddington limit¹ of the primary, with $\dot{M}_2/\dot{M}_1 = 10$, the characteristic temperatures of the three disks are

$$\begin{aligned} kT_{\text{outer}} &\simeq 28 \text{ eV} \\ kT_1 &\simeq 41 \text{ eV} \\ kT_2 &\simeq 1.3 \text{ keV} . \end{aligned}$$

The secondary black hole has a more compact disk, and typically accretes faster, so the secondary disk emission is bluer and brighter than the primary and outer disks.

Fig. 1 shows a toy model spectrum based on this picture and the temperature profiles in Eqn. 3. The inner disk extends to $r = a$ and the secondary disk extends to the Hill radius $r_H \simeq a(q/3)^{1/3}$. The outer disk starts at $r = a$, and extends to infinity. The preferential accretion parameter is set at $\dot{M}_2/\dot{M}_1 = 10$. The spectrum is double-peaked, with the UV and X-ray bumps formed by the outer and secondary disks respectively. The inner disk is out-shined by the other components, a consequence of the secondary black hole dominating

¹ This would imply the secondary accretes in a super-Eddington regime. This assumption is not crucial to our analysis, but it is interesting to keep in mind that \dot{M}_2/\dot{M}_1 might be kept smaller by radiative feedback.

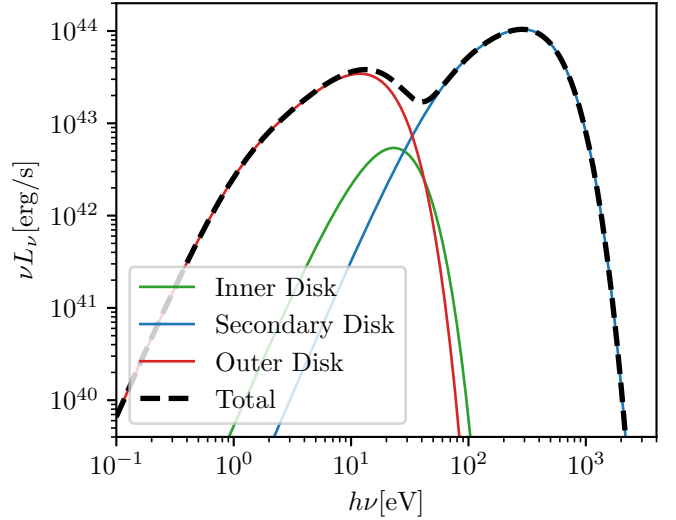


Figure 1. Toy model of the spectral energy distribution of thermal emission produced by an accretion flow around a $M = 10^7 M_\odot$ binary with mass ratio $q = 0.01$. The model assumes that the three components of the accretion flow: inner disk (green), secondary disk (blue), and outer disk (red) can each be characterized as a steady state α -disk, with radial temperature profile consistent with Eqn. 3.

the accretion. Note that a double-peaked spectrum similar to that shown in Fig. 1 is also presented in Chang et al. (2010), but the reason is different. In that study the secondary does not accrete, and the two spectral bumps are produced by the inner and outer disks.

2.3 Viscous Decoupling Timescale

At some point during the GW inspiral, the GW contraction rate τ^{-1} exceeds the viscous relaxation rate (e.g. Liu et al. 2003; Milosavljević & Phinney 2005). After that time, the disk is said to have “viscously decoupled” from the binary, as it can no longer spread viscously inwards as fast as the speed \dot{a}_{gw} of the binary contraction. Secular evolution of the brightness and color of the accretion flow around the binary could be significantly altered by the viscous decoupling. Note, that previous works (e.g. Sesana et al. 2012) have referred to this timescale as the “disk freezing timescale.” Also, the term “decoupling timescale” has been used in other works to refer to the time after which the GW power exceeds the rate of energy loss to tidal interactions with the disk. In this paper we refer to the transition from gas to GW driving as the “transition timescale.” The transition timescale is estimated later in Sec. 2.5.

The nominal viscous relaxation timescale of the accretion disk is given by

$$t_{\text{visc}}(r) = \frac{2}{3} \frac{r^2}{\nu(r)}, \quad (4)$$

where $\nu(r)$ is the kinematic viscosity at radius r . In a standard α -disk with constant aspect ratio h/r , the viscosity coefficient can be written as $\nu(r) = \bar{\nu}\sqrt{GM}r$. Here $\bar{\nu} \equiv \alpha/\mathcal{M}^2$, where $\alpha \lesssim 0.1$ represents the Reynolds stress associated with small-scale (numerically unresolved) turbulence in the disk (Shakura & Sunyaev 1973), and \mathcal{M} is the orbital Mach number. In addition to the fiducial binary parameters introduced in Sec. 2.1, we also define a set of fiducial disk parameters $\alpha = 0.1$ and $\mathcal{M} = 10$.

The ratio of the viscous time near the binary to the GW inspiral

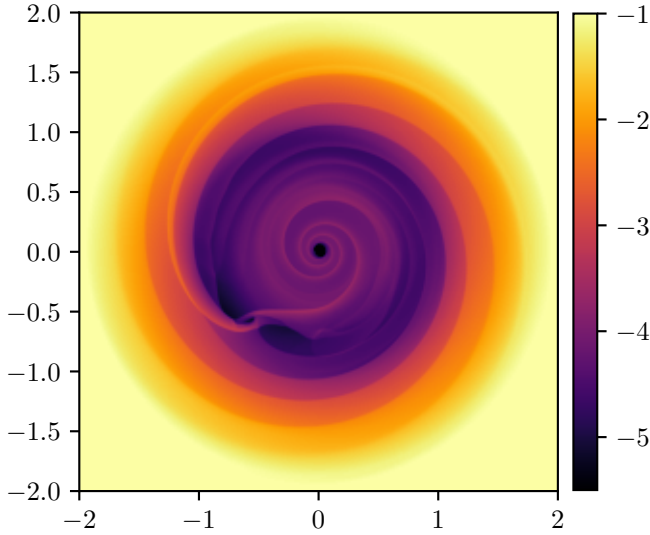


Figure 2. Image of the surface density of the disk around the MBHB with mass ratio $q = 0.01$, accreting from a circumbinary gas disk. The image is from a simulation snapshot taken well after the disk is viscously relaxed, but before the binary separation has been reduced much from a_0 . The axes show the $x - y$ plane in units of a_0 .

time is

$$\frac{t_{\text{visc}}(a)}{\tau} = \frac{128G^3 M^3 \eta}{15\nu(a)c^5 a^2} \propto a^{-5/2}. \quad (5)$$

This ratio starts off small and grows larger as the inspiral proceeds. It exceeds unity at the viscous decoupling radius a_{dec} ,

$$\begin{aligned} a_{\text{dec}} &= r_g \left(\frac{128\eta}{15\bar{\nu}} \right)^{2/5} \\ &\simeq 0.6 \text{ AU} \times \left(\frac{M}{10^7 M_\odot} \right) \left(\frac{\eta}{10^{-2}} \right)^{2/5} \left(\frac{\bar{\nu}}{10^{-3}} \right)^{-2/5}, \end{aligned} \quad (6)$$

which we have written here, first in terms of r_g , and then for a typical *LISA* binary with the fiducial parameters described in Sec. 2.1. The residence time for that system at the viscous decoupling stage is

$$\begin{aligned} \tau_{\text{dec}} &= \frac{5}{64} \frac{r_g}{c\eta} \left(\frac{128\eta}{15\bar{\nu}} \right)^{8/5} \\ &\simeq 5.4 \text{ days} \times \left(\frac{M}{10^7 M_\odot} \right) \left(\frac{\eta}{10^{-2}} \right)^{3/5} \left(\frac{\bar{\nu}}{10^{-3}} \right)^{-8/5}, \end{aligned} \quad (7)$$

which corresponds to a time-to-coalescence of $t_{\text{minus}} \simeq 1.4$ days. The orbital period at the viscous decoupling radius is

$$P_{\text{dec}} = 1.2 \text{ hours} \times \left(\frac{M}{10^7 M_\odot} \right) \left(\frac{\eta}{10^{-2}} \right)^{3/5} \left(\frac{\bar{\nu}}{10^{-3}} \right)^{-3/5}. \quad (8)$$

Eqn. 7 shows the timescale at which the binary is generally expected to become starved of mass supply. Note the apparent high sensitivity to the viscosity suggests that thinner α -disks might viscously decouple much earlier than warmer disks; if $\bar{\nu}$ were instead 10^{-5} ($M = 100$), Eqn. 7 indicates the viscous decoupling timescale would then be on the order of years rather than days. In Sec. 4.2 we show that this expectation is not supported by our simulations; we find instead that viscous decoupling extends over thousands of τ_{dec} , implying that colder and warmer disks alike could show signs of the inspiral long before the nominal decoupling time.

Measurements of the preferential accretion parameter \dot{M}_2/\dot{M}_1 are

reported in a number of studies (Lubow et al. 1999; Young & Clarke 2015; Muñoz et al. 2020; Duffell et al. 2020; Siwek et al. 2023a), and these generally find values of \dot{M}_2/\dot{M}_1 in the range of 1 – 10, when the mass ratio is larger than roughly 10^{-3} . All of those studies were based on simulations with a viscously relaxed disk. In Sec. 4.2 we present calculations revealing how the preferential accretion parameter evolves throughout the long-term viscous decoupling.

2.4 An Argument Against Tidal Squeezing

As the disk loses its viscous coupling to the binary, the feeding rates \dot{M}_1 and \dot{M}_2 evolve away from their steady state values. These long-term trends will largely determine the IMRI brightness and color evolution before coalescence. However the feeding rates are not easy to predict without detailed simulations. The main question here is whether the GW burst is preceded by a period of AGN brightening, or dimming. Armitage & Natarajan (2002) computed the evolution of a one-dimensional Keplerian disk, with an embedded low-mass secondary black hole ($q = 0.01$) on a GW-driven inspiral. They accounted for the tidal torque of the secondary on the inner and outer disks, using a prescription for Lindblad torques due to Lin & Papaloizou (1986). That prescription leads to the formation of an evacuated gap around the secondary orbit, which fully insulates the mass flow between the inner and outer disks and prohibits any movement of gas onto the secondary black hole. The result, which can be seen for example in Fig. 3 in Armitage & Natarajan (2002), is that the inner disk is squeezed toward the primary as the secondary spirals in.

Tidal squeezing would require the secondary to exert sufficient gravitational torque to the inner disk, to lower the orbits of gas parcels faster than \dot{a}_{gw} . It implies the positive torque, \dot{J}_{in} , exerted by the inner disk on the secondary, must exceed

$$\dot{J}_{\text{plow}} \equiv \pi a^2 \Sigma(a) \times \Omega(a) a^2 / \tau_{\text{gw}} \simeq \frac{64\eta \dot{M} r_g^3 c}{15\bar{\nu} a^2}, \quad (9)$$

where the second equality is precise in a steady state with $\dot{M} = 3\pi\nu(r)\Sigma(r)$. The dependence of this torque on a^{-2} indicates that to squeeze the inner disk would require the torque to diverge leading up to merger. The tidal torque coming from the inner disk can be written as $\dot{J}_{\text{in}} = \ell_{\text{in}} J_2 \dot{M}/M$ where $J_2 \simeq M_2 \Omega a^2$ is the secondary angular momentum, and ℓ_{in} is a dimensionless “eigenvalue”, which is typically not greater in magnitude than about 10 (Muñoz et al. 2020; Duffell et al. 2020; Tiede et al. 2020). It is then straightforward to see that \dot{J}_{plow} (the torque required to squeeze the inner disk) exceeds \dot{J}_2 some $1/(6\pi\eta\bar{\nu}\ell_{\text{in}})$ orbits before merger. In the fiducial binary and disk system with $\eta \simeq 0.01$, $\bar{\nu} = 10^{-3}$, and torque eigenvalue of order unity, this corresponds to ~ 5000 orbits or ~ 25 years before merger. Thus, on dynamical grounds, we expect that in the final thousands of orbits, the inner disk gas is either funneled to the outer disk, or falls onto the secondary. It would require an unrealistically large tidal torque to confine the inner disk inside the secondary’s orbit in the late inspiral. In Sec. 4.6 we present numerical calculations confirming these estimates.

2.5 Transition From Gas to GW Driving

For much of the binary lifetime, the orbital contraction is thought to be governed by coupling to the circumbinary disk (Begelman et al. 1980, e.g.). As the binary contracts and the GW power increases, there is a transition from gas to GW driving (Escala et al. 2005; Lodato et al. 2009; Cuadra et al. 2009; Muñoz et al. 2020; Bortolas et al.

2021). Once the binary reaches that separation, which we denote here as a_{trans} , an inspiral towards merger is inevitable as GW's remove orbital energy from the binary at a runaway rate. Note that some authors use different terminology for this separation and timescale, for example [Sesana et al. \(2012\)](#) simply calls this ‘‘decoupling.’’ We adopted the term ‘‘transition separation’’ for the switch to GW driving, in order to reserve the term decoupling for the process of viscous decoupling.

The transition separation occurs where the rate of orbital contraction by GW radiation (Eqn. 1) is equivalent to the rate of orbital contraction by gas i.e. $\dot{a}_{\text{gas}} = \dot{a}_{\text{gw}}$. Gas-induced changes of the semi-major axis are prescribed here in terms of another dimensionless constant $\epsilon \sim 1$, as $\dot{a}_{\text{gas}} = -\epsilon a \dot{M}/M$. Equating \dot{a}_{gw} and \dot{a}_{gas} , we find the separation at which GW's begin to dominate the inspiral,

$$\begin{aligned} a_{\text{trans}} &= r_g \left(\frac{64\eta c^3}{5G\dot{M}\epsilon} \right)^{1/4} \\ &\simeq 140 \text{ AU} \times \left(\frac{M}{10^7 M_\odot} \right)^{3/4} \left(\frac{\eta}{10^{-2}} \right)^{1/4} \epsilon^{-1/4} \dot{m}^{-1/4}, \end{aligned} \quad (10)$$

where $\dot{m} \equiv \dot{M}/\dot{M}_{\text{edd}}$ is the mass accretion rate normalized by the Eddington accretion rate. The timescale for the transition from gas to GW-driven inspiral is $\tau_{\text{trans}} \equiv \tau(a_{\text{trans}}) = t_{\text{sal}}/\epsilon\dot{m}$, where $t_{\text{sal}} = 5 \times 10^7$ years is the Salpeter time.

This implies that *LISA* inspirals will be generally deep in the GW-driven regime, and it justifies the choice of circular binary orbits in this study. Even though a detectable level of orbital eccentricity could be left over from a gas-driven evolutionary phase in *LISA* sources ([Armitage & Natarajan 2005](#); [Roedig et al. 2011](#); [Zrake et al. 2021](#); [Siwek et al. 2023b](#); [Garg et al. 2024](#); [Valli et al. 2024](#)), from the point of view of the circumbinary disk interaction years before a merger, the orbit can be considered as nearly circular.

2.6 Post-Merger Viscous Closing

Viscous decoupling implies the binary merges in a relatively low-density ‘‘hole’’ in the disk. Here we estimate the timescale for the hole to be refilled following the merger, noting that such effect has been surmised to lead to a late-time brightening, or ‘‘merger afterglow’’ (e.g. [Milosavljević & Phinney 2005](#)). The afterglow is predicted to begin a time span t_{refill} following the merger, given by the viscous relaxation timescale at the radius where the binary became viscously decoupled,

$$\begin{aligned} t_{\text{refill}} &\equiv \frac{3}{4} t_{\text{visc}}(a_{\text{dec}}) = \frac{1}{2} \frac{r_g}{c\bar{v}} \left(\frac{128\eta}{15\bar{v}} \right)^{3/5} \\ &\simeq 4.1 \text{ days} \times \left(\frac{M}{10^7 M_\odot} \right) \left(\frac{\eta}{10^{-2}} \right)^{3/5} \left(\frac{\bar{v}}{10^{-3}} \right)^{-8/5}. \end{aligned} \quad (11)$$

This estimate is analogous to one given in [Milosavljević & Phinney \(2005\)](#). Note that it suggest the remnant black hole begins refueling on a timescale that is quite sensitive to the disk viscosity; in an α -viscosity model, the refueling timescale would appear to increase from days for $M = 10$ to decades for $M = 100$. We show in Sec. 4.3 that such sensitivity is not supported by the simulations, instead the remnant begins fueling over year-like timescales, with surprisingly little sensitivity to the amplitude of the effective viscous stress.

2.7 Importance of Self-Gravity

Our simulations do not include the self-gravity of the disk gas, so it is important to check when that assumption could be valid. The importance of self-gravity can be estimated from the Toomre parameter,

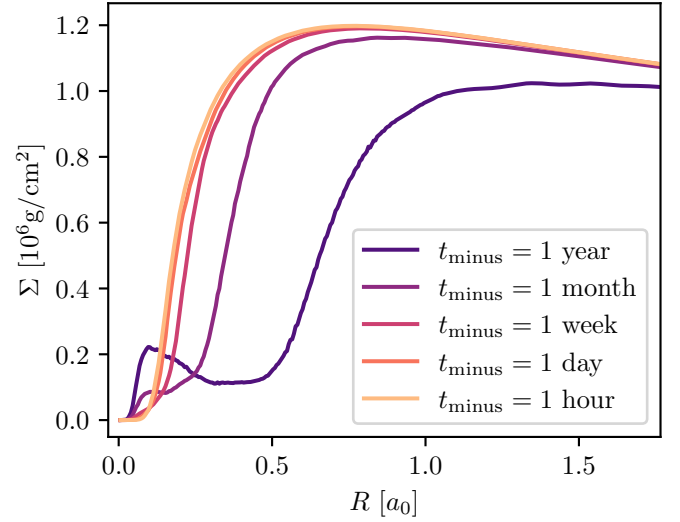


Figure 3. The radial profile of the surface density $\Sigma(r)$ in a binary with mass ratio $q = 0.01$ and orbital Mach number $M = 10$, shown at representative times before the merger. The radial profiles are obtained from the azimuthal average of the two-dimensional disk surface density.

$Q = c_s \kappa / \pi G \Sigma$; disks are generally unstable to fragmentation instabilities if $Q \lesssim 1$. When $\alpha = 0.1$ and $M = 10$ the Toomre parameter is found to be

$$Q = 6 \times 10^5 \left(\frac{M}{10^7 M_\odot} \right)^{1/2} \left(\frac{\bar{v}}{10^{-3}} \right) \left(\frac{r}{10a} \right)^{-3/2} \dot{m}. \quad (12)$$

Colder disks are more unstable to gravitational fragmentation, however Eqn. 12 indicates that even when the Mach number is on the order of hundreds, the disk still has $Q \gg 1$ out to $r \sim 10a$. The effect of gravitational instabilities on long-term binary orbital evolution has been examined in e.g. [Franchini et al. \(2021\)](#); [Bortolas et al. \(2021\)](#). Self-gravity is not likely to influence the EM signatures of the late inspiral.

3 NUMERICAL METHODS

Our hydrodynamic simulations are performed using the publicly available *Sailfish* code. *Sailfish* is a GPU-accelerated, second-order grid-based hydrodynamics code, with physics and post-processing features specifically targeting problems related to binary-disk interactions. It has been used in many published studies of binary accretion (e.g. [Zrake et al. 2021](#); [Tiede et al. 2020, 2022](#); [Westernacher-Schneider et al. 2022, 2024](#); [Krauth et al. 2023a,b](#); [Duffell et al. 2024](#); [Tiede & D’Orazio 2024](#); [DeLaurentiis et al. 2024](#)).

3.1 Equations of Motion

Our simulations are based on solutions to the vertically-averaged, time-dependent mass continuity and Navier-Stokes equations,

$$\frac{\partial \Sigma}{\partial t} + \nabla \cdot (\Sigma \mathbf{v}) = \dot{\Sigma}_{\text{sink}}, \quad (13)$$

$$\frac{\partial \Sigma \mathbf{v}}{\partial t} + \nabla \cdot (\Sigma \mathbf{v} \mathbf{v} + P \mathbf{I} - \mathbf{T}_{\text{vis}}) = \dot{\Sigma}_{\text{sink}} \mathbf{v} + \mathbf{F}_g. \quad (14)$$

Here, Σ is the vertically-integrated mass density, \mathbf{v} is the gas velocity, $P \equiv \Sigma c_s^2$ is the vertically-integrated gas pressure, and \mathbf{I} is the identity

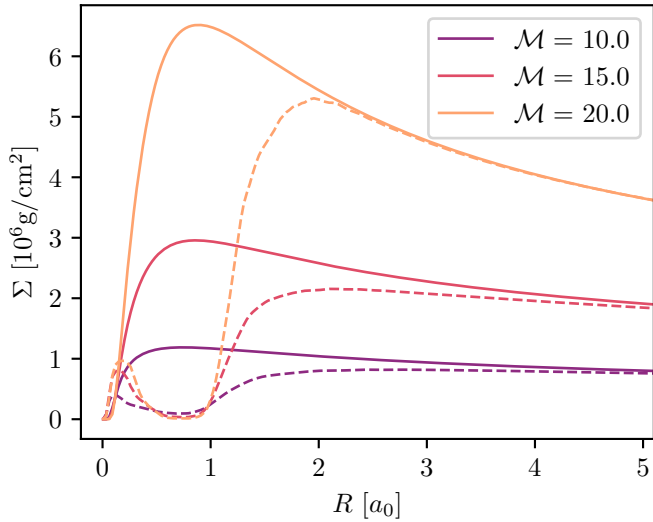


Figure 4. The radial profile of the surface density $\Sigma(r)$ in a binary with mass ratio $q = 0.01$ and orbital Mach numbers in the range $M = 10, 15, 20$, shown at 4000 orbits before merger (dashed) and at merger (solid). The radial profiles are obtained from the azimuthal average of the two-dimensional disk surface density.

tensor (pressure is isotropic). We adopt the locally isothermal equation of state, $c_s^2 = -\phi/M^2$, where M is the orbital Mach number, and the gravitational potential is given by

$$\phi = -\frac{GM_1}{(r_1^2 + r_s^2)^{1/2}} - \frac{GM_2}{(r_2^2 + r_s^2)^{1/2}}. \quad (15)$$

Here r_1 and r_2 are the distances to each black hole and r_s is the gravitational softening length to ensure the potential is finite at the component positions. Use of the locally isothermal equation of state means that we do not solve an energy transport equation, nor adopt a phenomenological cooling prescription. Certain thermodynamic processes such as shock-heating are not accounted for as a result of the isothermal equation of state.

The “sink” term $\dot{\Sigma}_{\text{sink}}$, appearing in Eqns. 13 and 14, is responsible for the direct exchange of mass and momentum between the gas and the binary components,

$$\dot{\Sigma}_{\text{sink}} = -\frac{\Sigma}{\tau_{\text{sink}}} \left(e^{-r_1^2/2r_{\text{sink}}^2} + e^{-r_2^2/2r_{\text{sink}}^2} \right). \quad (16)$$

The choice of the sink rate τ_{sink} does not significantly alter the results, as long as it is chosen to be comparable to or larger than the viscous rate at the sink radius (Moody et al. 2019; Tiede et al. 2020; D’Orazio & Duffell 2021; Duffell et al. 2024). $\mathbf{F}_g = -\Sigma \nabla \phi$ is the vertically integrated gravitational force density, associated with the softened gravitational potential. We assume the binary mass $M = M_1 + M_2$ is much larger than the disk mass, so that self-gravity can be safely ignored (see Sec. 2.7).

The components of the viscous stress tensor \mathbf{T}_{vis} in Eqn. 14 are given by $T_{\text{vis}}^{ij} = \nu \Sigma \left(\partial^j v^i + \partial^i v^j - \partial_k v^k \delta^{ij} \right)$. *Sailfish* supports both “constant- ν ” and “constant- α ” viscosity prescriptions. For this study we have adopted the constant- α viscosity prescription, with kinematic viscosity coefficient

$$\nu = \frac{\alpha c_s^2}{\tilde{\Omega}}, \quad (17)$$

where the modified Keplerian orbital frequency $\tilde{\Omega}$ is

$$\tilde{\Omega} = \sqrt{\frac{GM_1}{r_1^3} + \frac{GM_2}{r_2^3}}. \quad (18)$$

At large radii $r \gg a$, Eqn. 17 reduces to $\nu \approx \bar{\nu} \sqrt{GM} r$ where $\bar{\nu} = \alpha/M^2$.

The black holes are moved according to the Kepler two-body problem, modified to account for the GW-driven inspiral up to the leading post-Newtonian order (Peters 1964). The semi-major axis as a function of time is the solution of Eqn. 1,

$$a(t) = a_0 (1 - 4t/\tau_0)^{1/4}, \quad (19)$$

where τ_0 is the contraction timescale at the start of the simulation. To position the binary components on the grid requires an expression for the orbital phase $\phi(t)$ as a function of the simulation time t . The orbital phase is obtained by integrating in time the instantaneous orbital frequency,

$$\phi(t) = \int_{a_0}^{a(t)} \sqrt{\frac{GM}{a^3}} \frac{da}{\dot{a}_{\text{gw}}} = \frac{2}{5} \tau_0 \Omega_0 \left(1 - \left(\frac{a(t)}{a_0} \right)^{5/2} \right). \quad (20)$$

The gravitational force of the gas is neglected in the binary equation of motion, which is justified because we are only considering binaries deep in the GW-driven regime.

3.2 Initial Data, Outer Boundary Condition, and Diagnostics

We start our simulations of accretion onto the binary with a circular gas disk: the azimuthal velocity profile is $v_\phi = v_{\text{kep}} = \sqrt{GM/r}$, the radial velocity is inward at the viscous drift speed, $v_r = -3\nu(r)/2r$, and the surface density is that of a steady state α -disk,

$$\Sigma_0(r) = \frac{\dot{M}_0}{3\pi\nu(r)} \propto r^{-1/2}. \quad (21)$$

Note that Eqn. 21 is the surface density of a steady disk with a zero net angular momentum current, this fact is revisited in Sec. 3.3. After the start of the simulation, it takes several viscous timescales at $r \sim a_0$ for the flow to relax to a statistically steady state. For reference, when $\alpha = 0.05$ and $M = 10$, the viscous timescale at $r = a_0$ is $t_{\text{visc}} \approx 200$ orbits. Fig. 2 shows a snapshot of the surface density once the system has viscously relaxed to a quasi-steady state.

Because our code uses Cartesian coordinates with a square-shaped domain, we impose a “soft” outer boundary condition, within a circular buffer zone starting at radius $r_{\text{buf}} \approx 7.5a_0$ (we have confirmed that our results are not changed by an increase of r_{buf} , see Sec. 3.3). Inside the buffer region, the surface density and gas velocity are driven smoothly toward a zero-torque α -disk (which is also the initial condition). The domain size of our simulations is $20a_0$ and the number of grid zones is 2400×2400 , unless mentioned otherwise; the simulations considered in this paper have grid spacing $\Delta x \approx 0.008a_0$.

The accretion rate for each black hole is measured by separately integrating the two terms in Eqn. 16 corresponding to the primary and secondary black hole accretion rates. Smoothing is applied to the time series of the accretion rates unless specifically mentioned. Time series of the tidal torque is computed by integrating the gravitational torque density over the whole surface of the disk. It is decomposed into the torque on the primary, or the secondary, and also into contributions from the inner and outer disks.

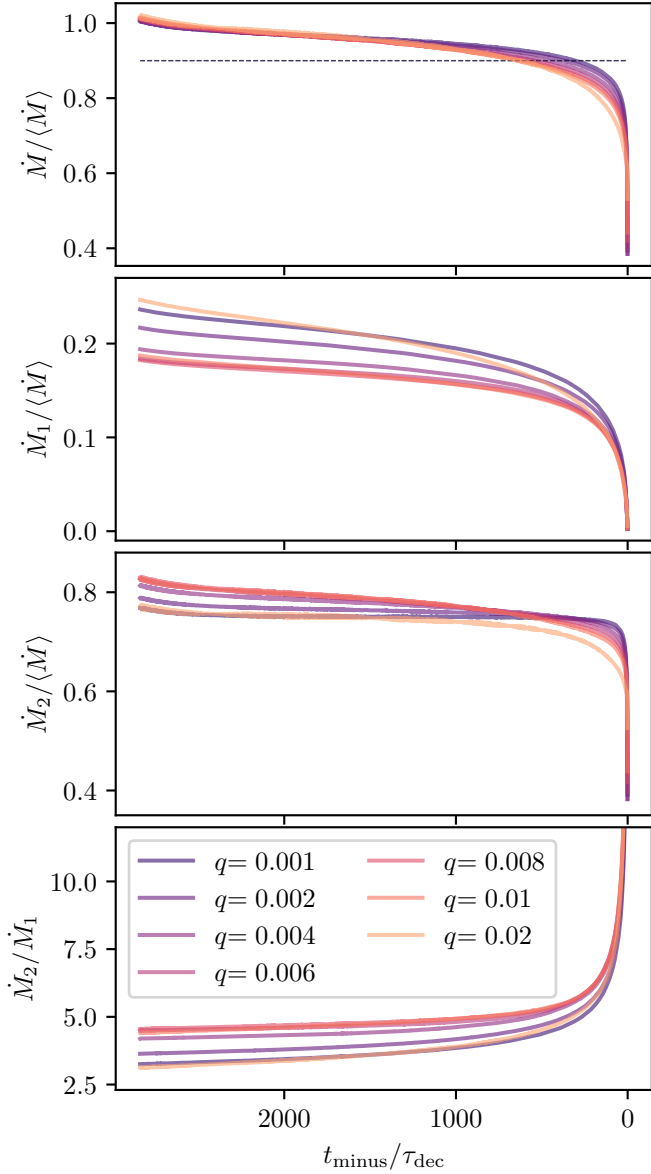


Figure 5. Time series of the mass accretion rates \dot{M} (top), \dot{M}_1 (second), \dot{M}_2 (third) and the preferential accretion parameter \dot{M}_2/\dot{M}_1 (bottom), for mass ratios q in the range of 0.001–0.02. The gas orbital Mach number is $\mathcal{M} = 10$. The dashed line in the top panel is where $\dot{M} = 0.9\langle\dot{M}\rangle$.

3.3 A Note About Accretion Rates in the Steady State

Ideally, our accretion rates \dot{M}_1 and \dot{M}_2 would be reported relative to the theoretical inflow rate \dot{M}_0 in Eqn. 21. However, we have observed that in our simulations, the mean binary accretion rate $\langle\dot{M}\rangle$ generally exceeds \dot{M}_0 by a significant margin. We understand this “overshoot” to be an artifact of our treatment of the domain outer boundary (Sec. 3.2).

Near the outer boundary (or the buffer region), the surface density is driven smoothly toward $\Sigma_0(r)$ in Eqn. 21, which corresponds to a zero-torque disk. We make this choice mainly for convenience, because the torque on the binary \dot{J} cannot be controlled, rather it needs to be measured from the simulation. When \dot{J} is positive, a better approximation of the surface density far from the binary is

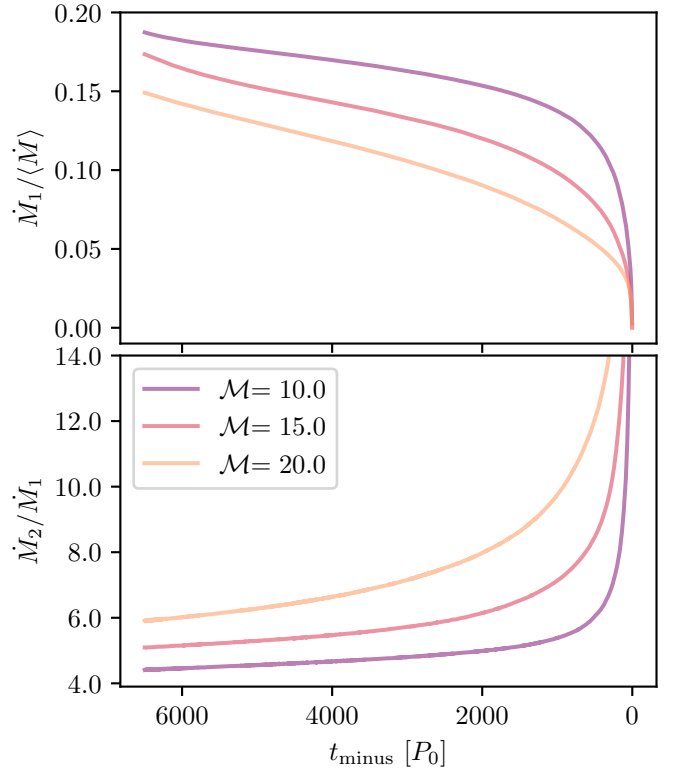


Figure 6. Time series of the mass accretion rates \dot{M}_1 (top) and the preferential accretion parameter \dot{M}_2/\dot{M}_1 (bottom), for a range of Mach numbers $\mathcal{M} = 10, 15, 20$. The binary mass ratio is $q = 0.01$. Each curve of the top panel is normalized by the empirical average binary accretion rate throughout the inspiral $\langle\dot{M}\rangle$.

(see e.g. Pringle 1981)

$$\Sigma(r) = \frac{1}{3\pi\nu(r)} \left(\langle\dot{M}\rangle - \frac{\dot{J}}{\sqrt{GM}r} \right). \quad (22)$$

Thus the target surface density $\Sigma_0(r)$ would be generally smaller than $\Sigma(r)$ if we had $\langle\dot{M}\rangle = \dot{M}_0$. However the buffer zone forces the equality $\Sigma(r_{\text{buf}}) = \Sigma_0(r_{\text{buf}})$, so in general we have $\langle\dot{M}\rangle \gtrsim \dot{M}_0$.

The amount of this “overshoot” can be estimated, noting that when the binary mass ratio is small, the gravitational torque is negligible, and the net angular momentum current is then $\dot{J} \simeq M_2\Omega a^2$. The ratio of the measured inflow rate $\langle\dot{M}\rangle$ to the nominal inflow rate \dot{M}_0 is then

$$\frac{\langle\dot{M}\rangle}{\dot{M}_0} \simeq \frac{1}{1 - \sqrt{a/r_{\text{buf}}}}. \quad (23)$$

In Eqn. 23 we have also assumed the secondary dominates a majority of the accretion, i.e. $\dot{M}_2 \simeq \langle\dot{M}\rangle$. In simulations where $r_{\text{buf}} = 7.5a_0$, Eqn. 23 predicts $\langle\dot{M}\rangle/\dot{M}_0 \simeq 1.57$, which is very close to what we observe.

We have checked that the overshoot does not contaminate any of our derived science results, such as the shape of the accretion rate time series. Overshoots of the kind we observed here could be mitigated by guessing the value of \dot{J}/\dot{M} , and then driving the solution in the buffer region toward $\Sigma(r)$ in Eqn. 22. Note that overshoots of the binary accretion rate have also been reported in Farris et al. (2014) and Shi & Krolik (2015) and were also discussed in Rafikov (2016). We suggest here that the finite domain size could have been responsible for those observations.

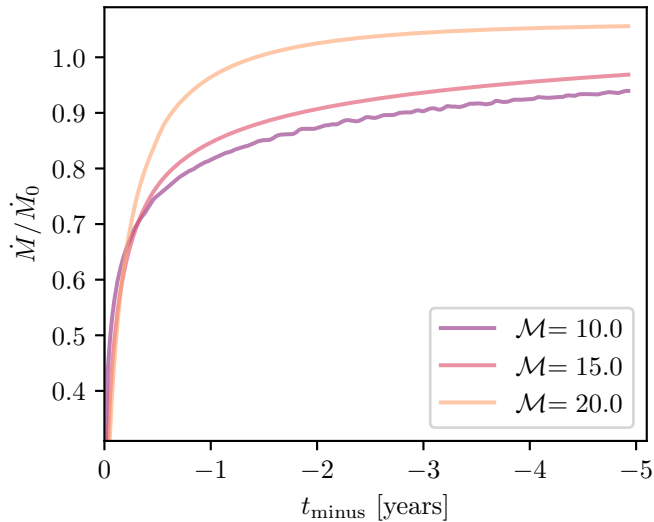


Figure 7. Time series of the post-merger mass accretion rate for the fiducial model, but with a range of Mach numbers $\mathcal{M} = 10, 15, 20$.

4 SIMULATION RESULTS

We simulated the GW-driven inspirals of black hole binaries with mass ratios between $q = 10^{-3}$ and $q = 10^{-1}$, surrounded by disks with orbital Mach numbers $\mathcal{M} = 10, 15, 20$. The binary mass is $M = 10^7 M_\odot$, however the accretion rate time series could be rescaled, by an appropriate remapping of the time coordinate, to describe a binary of any mass. Results related to observer time scales, EM light curves, and emission spectra depend on M , but they also scale with it in obvious ways. Simulations generally begin on the order of $\tau/P \sim 10^4$ binary orbits prior to the coalescence. In Sec. 4.7 we show that this provides sufficient time for the disk to relax, and “forget” the simulation initial condition well before the viscous decoupling stage. Times are measured in the binary rest-frame, not in the observer time, i.e. we do not adjust the time scales for cosmological redshift.

4.1 Evolution of Disk Surface Density

Fig. 3 shows the surface density radial profiles of the fiducial disk, initially at $t_{\text{minus}} = 1$ year and then at four other representative times leading up to merger. At radii $r \gtrsim a_0$, the surface density profile is approximately $\Sigma \propto r^{-1/2}$, as for a steady state α -disk in Eqn. 21. The surface density evolution is similar in certain ways to the one-dimensional disk model from Chang et al. (2010). An annular gap is formed around the secondary orbit, and the outer disk follows the secondary inwards up until the viscous decoupling time. However, the gap in our simulation is not fully evacuated; gas flows across the gap and accretes to the secondary. Also, the surface density of the inner disk in our simulation is seen to be modestly decreasing over time, whereas in Chang et al. (2010), the presence of the vacuum gap around the secondary orbit requires the surface density of the inner disk to increase. We show in the next sub-section, that the decrease of the inner disk mass is driven mainly by accretion to the secondary.

The surface density radial profiles for varying Mach number disks are shown in Fig. 4 at 4000 orbits before merger (dashed) and at merger (solid). For higher Mach number disks, we find that more gas is steeply piled up outside the secondary orbit as the outward angular momentum current \dot{J} and opposing accretion flow \dot{M} piles gas at the

inner edge of the outer disk. This effect is analogous to the greater buildup of gas at the inner rim of the circumbinary disk, seen for colder disks by Tiede et al. (2020) in the case of equal-mass binaries.

4.2 Long-Term Viscous Decoupling

Fig. 5 shows the binary accretion rate \dot{M} (top), the accretion rates to the binary components \dot{M}_1 and \dot{M}_2 (middle), and the preferential accretion rate \dot{M}_2/\dot{M}_1 (bottom). The curves show the time series data for binaries with various mass ratios. Our main results here can be summarized, (1) the secondary generally starves more slowly than the primary, and (2) the binary accretion rate \dot{M} shows a long-term downward trend, being reduced from $\langle \dot{M} \rangle$ by 10% as early as $\sim 500\tau_{\text{dec}}$ (decade-like time span) before the merger.

The second result is surprising, as one could reasonably guess that \dot{M} would be significantly reduced from \dot{M}_0 only within a few τ_{dec} of the merger, perhaps following a functional form like $\dot{M} = \dot{M}_0 e^{-\tau_{\text{dec}}/t_{\text{minus}}}$. Instead, our results suggest the quantity $\delta \equiv 1 - \dot{M}/\dot{M}_0$ might grow as a power law in t_{minus} , at least while δ is small. We summarize next a model of the viscous decoupling process, which does predict such scaling of δ . A proper derivation of the model will be reported separately, along with detailed comparisons to the simulation results presented here.

Our model characterizes the disk as having two distinct zones: a close zone that is tightly coupled to the binary, and a distant zone that is relatively frozen over the remaining time before the merger. The two zones meet at a viscous radius, r_v , satisfying $t_{\text{visc}}(r_v) = -a/\dot{a}_{\text{gw}}^2$. In the close zone $r < r_v$, the disk evolves through a sequence of steady states (Eqn. 22), each conducting angular momentum inward at rate $\dot{J} = \dot{M}\Omega a^2$. At each step n of the sequence, a boundary condition is imposed, $\Sigma_n(r_n) = \Sigma_{n-1}(r_n)$, where r_n is the viscous radius at step n . Such recursion leads to a first-order ordinary differential equation for δ , and the solutions go asymptotically as $\delta \propto t_{\text{minus}}^{-5/24}$. Such weak dependence of δ on t_{minus} could account for the long-term viscous decoupling seen in our simulations.

In Sec. 2.3, we estimated that the viscous decoupling timescale would be very sensitive to the Mach number of the disk, $\tau_{\text{dec}} \propto \mathcal{M}^{16/5}$. However, given our argument above, where δ scales as a power-law in t_{minus} , it seems reasonable to expect that the late-inspiral accretion rate curves might have only modest sensitivity to the Mach number. To test this, we ran a suite of simulations with a range of Mach numbers, $\mathcal{M} = 10, 15, 20$. The results appear in Fig. 6, and do confirm this expectation. The run with Mach 20 has a nominal viscous decoupling time roughly 10 times larger than the run with Mach 10, and yet the curves differ mainly by a vertical offset. The long-term decoupling effect seen here also seems to be present in simulations of equal-mass inspirals in e.g. Fig. 6 in Farris et al. (2014), or Fig. 3 of Dittmann et al. (2023).

4.3 Remnant Fueling

Equally important to the pre-merger accretion evolution is the post-merger remnant refueling where the disk viscously refills the cavity and accretes onto the merger remnant. In Sec. 2.6 we derived the refilling timescale t_{refill} (Eqn. 11) and found that for the fiducial

² This idea is inspired by Sec. 3.2 of Rafikov (2016), which defines a viscous radius, but in a different setting where the binary orbit is held fixed while the disk viscously adjusts to a new angular momentum current. The idea is also used in Sec. 5.6 of Duffell et al. (2024) to explain the damping of a startup transient in simulations of binary accretion initiated with a zero-torque disk.

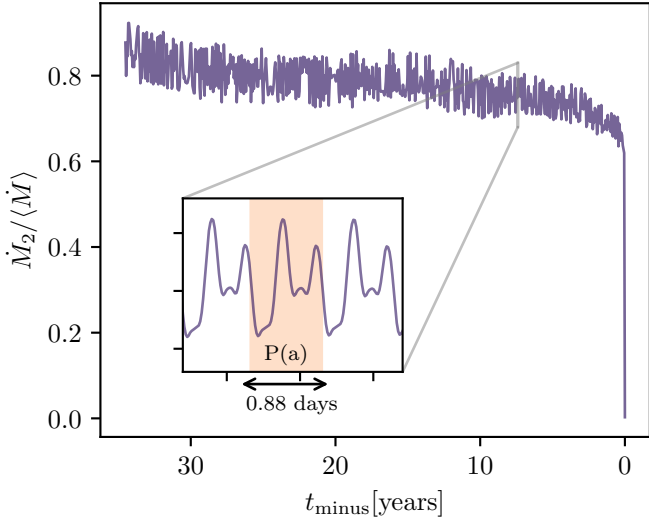


Figure 8. Time series of the secondary black hole mass accretion rate for a binary with mass ratio $q = 0.01$ and $\mathcal{M} = 10$. The highlighted region in the inset plot is the (unsmoothed) accretion rate during one rest-frame binary orbit, roughly 0.9 days at $t_{\text{minus}} = 8$ years when $q = 0.01$.

binary, the disk should refill the cavity, and begin accreting to the black hole merger remnant roughly 4 days after the merger. Note however that our estimate predicts $t_{\text{refill}} \propto \mathcal{M}^{16/5}$, analogous to the viscous decoupling time scale τ_{dec} . It would imply that the onset of refueling could be delayed from days (Mach 10) to decades if the disk had a Mach number of 100.

In Fig. 7, we plot the total binary accretion rate post-merger out to 5 years after coalescence, for a binary with mass ratio $q = 0.01$, and for simulations with different Mach numbers. The result indicates that the onset of refueling happens over a time span of months to years, with relatively little sensitivity to our derived estimate for t_{refill} . We thus suggest that the refilling timescale post merger is not well represented by a time constant such as that given in Eqn. 11, as the recovery of the accretion rate to \dot{M}_0 does not show any exponential characteristics. The exact functional form of the refueling curve can be predicted from the model which we summarized in Sec. 4.2, and comparisons will be presented in a forthcoming paper.

4.4 Variability of Mass Accretion Rates

Low-mass ratio binaries have been found to accrete in a different dynamical regime than binaries of near-equal mass (D’Orazio et al. 2016), with the low-mass ratio regime being characterized by a smaller amplitude of stochastic variability in the mass accretion rates. This suggests that accreting IMRI’s could produce “cleaner” light curves, possibly making it easier to identify them based on EM periodicity, or color evolution, in the years before a merger. In this section, we show that the reduced stochasticity seen by D’Orazio et al. (2016) applies throughout a GW-driven inspiral.

The time series of the secondary accretion rate \dot{M}_2 is shown in Fig. 8 for a $q = 0.01$ binary, and in Fig. 9 for a $q = 0.1$ binary. The amplitude of the stochastic variability in \dot{M}_2 is less than roughly 10% for the case of $q = 0.01$ and greater than roughly 50% for the case of $q = 0.1$, which confirms there is a significant increase in the variability amplitude somewhere between $q = 0.01$ and $q = 0.1$, and that this change persists also in the late inspiral phase, at least before the viscous decoupling.

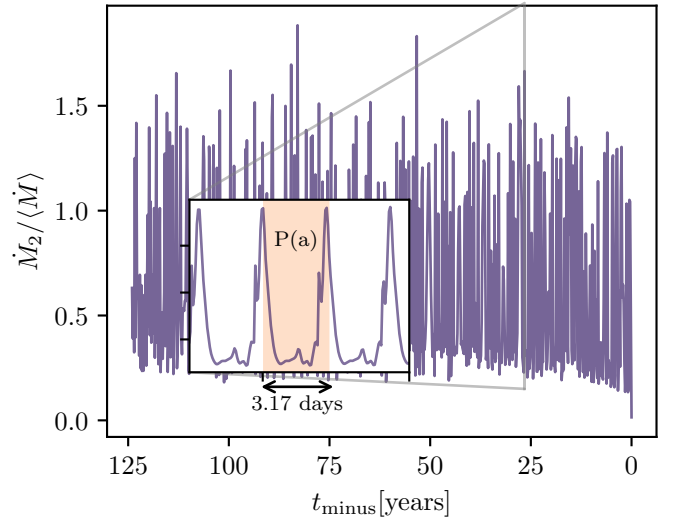


Figure 9. Time series of the secondary black hole mass accretion rate for a binary with mass ratio $q = 0.1$ and $\mathcal{M} = 10$. The highlighted region in the inset plot is the (unsmoothed) accretion rate during one rest-frame binary orbit, roughly 3.2 days at $t_{\text{minus}} = 25$ years when $q = 0.1$.

The periodic variability of unequal-mass systems can be seen in the insets of Figs. 8 and 9. The secondary accretion rate modulates at the binary orbital period, and we believe this must indicate a slight eccentricity of the outer disk (e.g. Kley & Dirksen 2006). For lower mass ratios, a second peak is noticeable in the secondary’s accretion rate. This feature could be produced by a standing wave, fixed in phase relative to the disk apsides, which the secondary passes through and accretes from once per orbit. Cocchiara et al. (2024) also report a second peak in the accretion rates and light curves of a circular binary with $q = 0.1$. As our study, using a grid-based code, and theirs using the hyper-Lagrangian code (Gizmo) both see the second peak feature, we believe that feature could be robust.

4.5 Evolution of Binary Torques

Fig. 10 shows the time series of the tidal torque on the binary for three mass ratios ($q = 0.002, 0.01, 0.02$). The top panel shows the non-dimensional torques $\ell_{\text{tot}} = (\dot{J}_{\text{tot}}/J)/(\dot{M}/M)$ and $\ell_{\text{in}} = (\dot{J}_{\text{in}}/J)/(\dot{M}/M)$, and the bottom panel shows the inner disk torque \dot{J}_{in} , normalized by $\dot{M}_0\sqrt{GMa_0}$. Fig. 11 shows the tidal torque on the binary for simulations of varying Mach number. The top panel shows the total gravitational torque exerted on the binary, and the middle and bottom panels show respectively the inner and outer disk contributions. Note in the top panel of Fig. 11 that the net tidal torque on the binary is negative for all of our runs, and that it becomes increasingly negative with increasing Mach number. This trend is consistent with other studies including Tiede et al. (2020) and Penzlin et al. (2022), which also find that the torque on the binary becomes increasingly negative with increasing Mach number. The outer disk is responsible for this increasingly negative torque at higher Mach number; the inner disk actually exerts a slightly positive torque on the binary, which is rather insensitive to the Mach number. The increasing magnitude of torque from the outer disk can be attributed to the accumulation of mass outside the secondary orbit (Fig. 4).

These results could be used to predict how the gravitational waveform of IMRI’s surrounded by gas should differ from those evolving

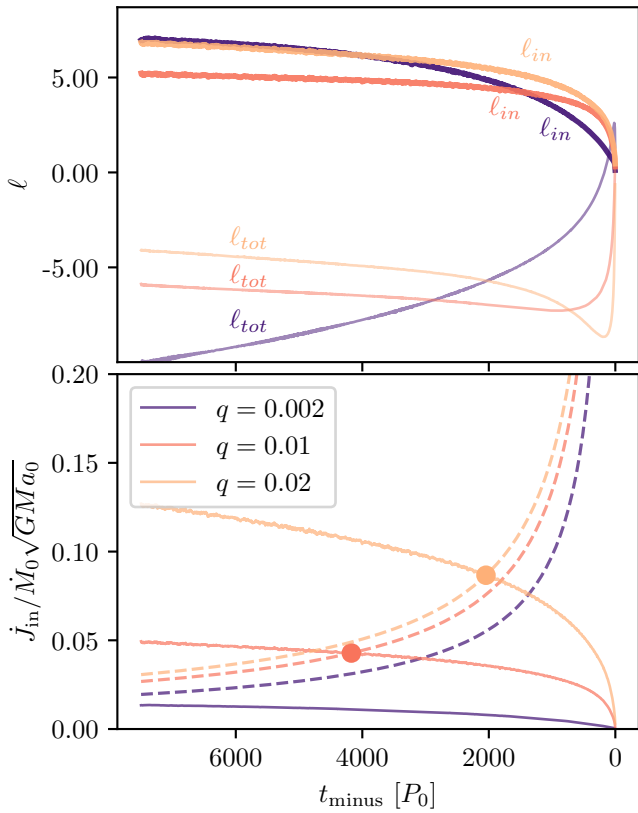


Figure 10. Evolution of the tidal torque, normalized in different ways, for mass ratios $q = 0.002, 0.01, 0.02$ and Mach number $\mathcal{M} = 10$. In the bottom panel, the solid lines are the measured torque \dot{J}_{in} , applied to the binary by the inner disk, the dashed lines show the minimum torque \dot{J}_{plow} (Eqn. 9), needed to sustain tidal squeezing, and the filled circles are where $\dot{J}_{\text{in}} = \dot{J}_{\text{plow}}$.

in vacuum (e.g. [Derdzinski et al. 2019, 2021](#); [Tiede et al. 2024](#)). Such predictions will be reported in a future study focusing specifically on GW signatures.

4.6 Tidal Squeezing of the Inner Disk

As discussed in Sec. 2.4, theory of disk-satellite interactions implies that the orbiting secondary generally exerts a retrograde torque to the inner disk. When prescriptions for that torque are utilized in a one-dimensional disk model, they can lead to the formation of a zero-density, insulating gap in the disk surrounding the secondary. If the secondary is on a GW-driven inspiral, the insulating gap then implies tidal squeezing of the inner disk (so-called “snowplow” mechanism), and a potentially dramatic enhancement of the accretion rate \dot{M}_1 to the primary in the very late inspiral. In Sec. 2.4 we referenced other studies which have observed that the insulating gap does not form in two-dimensional hydrodynamics calculations, and we also pointed out that the magnitude of the tidal torque, denoted as \dot{J}_{plow} , needed to reduce the inner disk radius at the rate \dot{a}_{gw} , diverges in the late inspiral. We report here the time series of tidal torque \dot{J}_{in} , applied to the binary by the inner disk (as well as \dot{J}_{tot} , the torque from the whole disk) and confirm our estimate from Sec. 2.4, that in the final thousands of orbits, \dot{J}_{in} is exceeded by \dot{J}_{plow} , meaning that tidal squeezing becomes ineffective well before the merger.

Fig. 10 shows time series data from the tidal torques on the binary, for three mass ratios ($q = 0.002, 0.01, 0.02$). The bottom panel shows

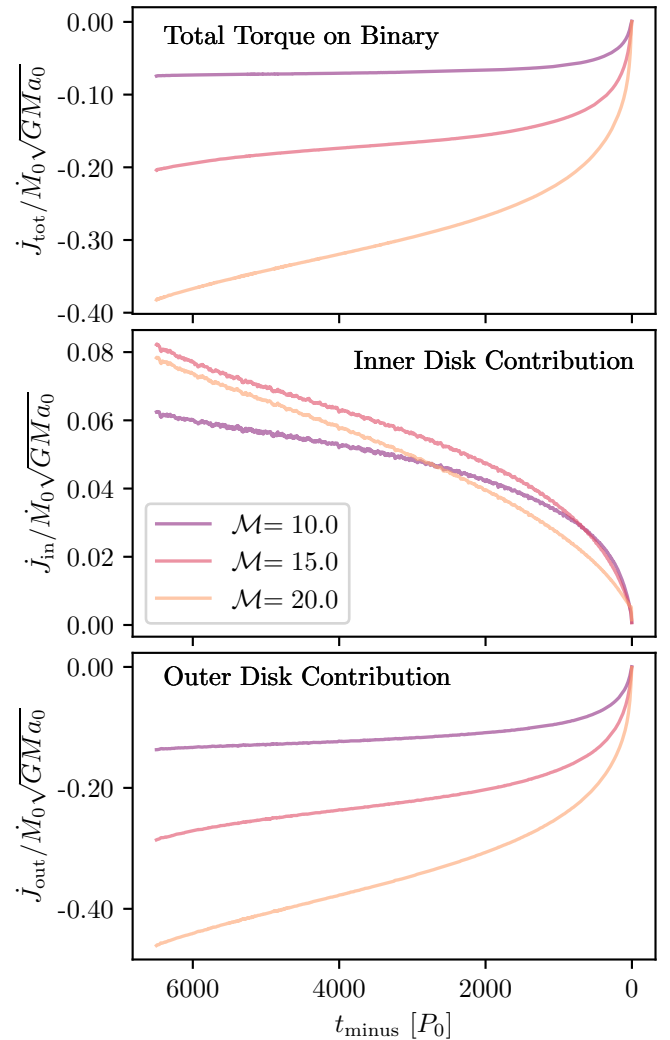


Figure 11. Evolution of the total gravitational torque \dot{J}_{tot} (top), inner disk torque \dot{J}_{in} (middle) and the outer disk torque \dot{J}_{out} (bottom) on the binary. The mass ratio is $q = 0.01$ and the Mach numbers are $\mathcal{M} = 10, 15, 20$.

\dot{J}_{in} (solid) and \dot{J}_{plow} (dashed) as derived in Eqn. 9. The filled in circles are where $\dot{J}_{\text{in}} = \dot{J}_{\text{plow}}$. Notice that \dot{J}_{plow} diverges close to merger; the secondary black hole can not provide enough torque to squeeze the inner disk in the final ~ 4000 orbits, consistent with the estimate given in Sec. 2.4. The top panel of Fig. 10 confirms an assumption we made in that estimate, that the non-dimensional torques do not change radically throughout the inspiral.

4.7 Numerical Convergence

We ran many simulations to check the sensitivity of our results to numerical parameters, including the grid resolution and the start time of the simulation relative to the binary merger. Fig. 12 presents the accretion rates of the fiducial binary for four simulations with different start times. The startup transients settle after roughly a hundred to a thousand orbits, and henceforth the accretion rates show very little sensitivity to the simulation start time. Also in Fig. 12 we have plotted the total accretion rate for a fiducial binary that is not inspiraling. This also helps assure us that the long-term viscous

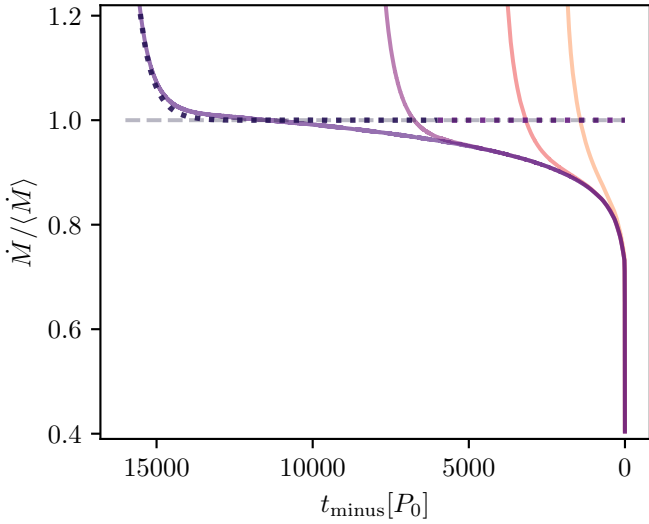


Figure 12. Time series of the binary mass accretion rate for mass ratio $q = 0.01$ and orbital Mach number $\mathcal{M} = 10$. The curves are from distinct runs initiated progressively earlier in the inspiral. The dotted line shows the accretion rate time series for a non-inspiraling binary.

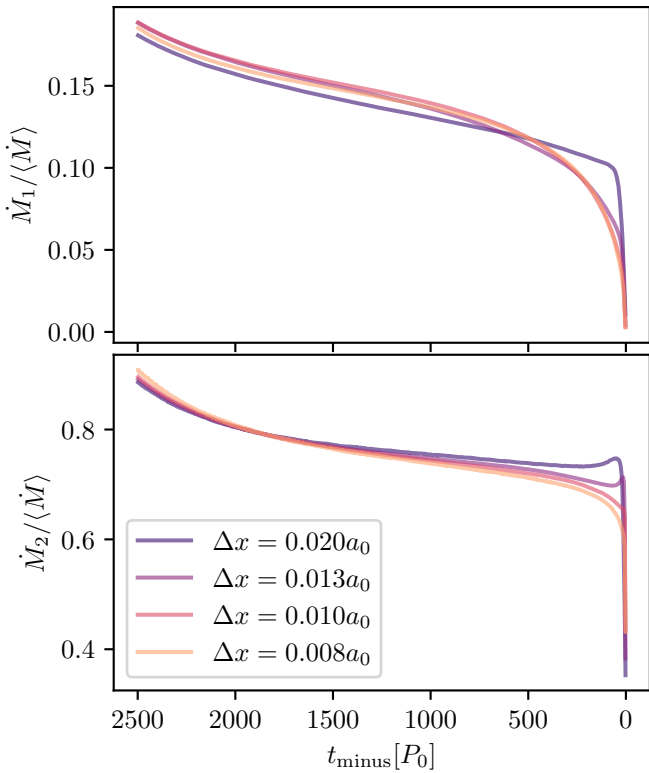


Figure 13. Time series of the mass accretion rates \dot{M}_1 (top) and \dot{M}_2 (bottom), for distinct runs grid spacings Δx in the range of $0.008a_0 - 0.02a_0$. The mass ratio is $q = 0.01$ and orbital Mach number is $\mathcal{M} = 10$. The accretion rate is normalized by the empirical average binary accretion rate throughout the inspiral $\langle\dot{M}\rangle$.

decoupling discussed in Sec. 2.3 is uniquely a consequence of the inspiraling binary.

We also checked that our accretion rate time series data is well converged with respect to the grid resolution, by plotting in Fig. 13 the accretion rates for simulations performed with different resolutions. Resolution is quantified by the grid spacing $\Delta x/a_0$ (better resolution means smaller Δx). Some disagreement is seen in both \dot{M}_1 and \dot{M}_2 when the resolution is worse than $\Delta x \simeq 0.01a_0$, especially in the very late inspiral stage when the distance between the binary components becomes poorly resolved. However at early times, the shapes of the accretion rate curves are reasonably consistent with one another when the resolution better than $\Delta x \simeq 0.01a_0$.

5 ELECTROMAGNETIC SIGNATURES

The inspiral of MBHB's might produce tell-tale EM signatures. The detections of such EM signatures by observatories including *Roman*, *Vera Rubin*, *UVEX*, *Athena*, or *eROSITA*, especially alongside a GW detection by *LISA*, would provide an abundance of knowledge on binary evolution, accretion, and environments of MBHB's within galaxies. To maximize the likelihood of an EM detection, we must understand how the hydrodynamical interactions between the binary and disk affect the thermal radiation released from the accretion flow. In this section we use the spectral toy model from Sec. 2.2, combined with the measured mass accretion rates, to provide a reasonable first approximation of the brightness and color evolution of an accretion flow surrounding an inspiraling black hole binary of significantly unequal mass.

5.1 Spectral Evolution and Light Curves

In Fig. 14 we plot the composite spectral energy distribution of the accretion flow in the fiducial binary simulation, at different times throughout the inspiral. We used the three-disk toy model from Sec. 2.2, in which the spectrum is computed by approximating each disk (inner, secondary, and outer) to emit as a blackbody. The inner cutoff radii for the inner and secondary disk are $R_i = 6GM_i/c^2$, the innermost stable circular orbits of the respective black hole components. The inner radius of the outer disk, and the outer radius of the inner disk, are set to the instantaneous separation of the binary, while the secondary disk is extended to the instantaneous Hill radius. The result is not sensitive to the outer radius of the outer disk.

In Fig. 15 we plot the UV (pink) and soft X-ray (orange) light curves, derived from our three-disk toy model of the disk temperatures. We define the UV energy range as 3.3 – 100 eV and the soft X-ray energy range as 0.25 – 5 keV. Note that we have manually imposed in our model to stall the inner edge of the outer disk at the decoupling separation. This is the reason for the abrupt change in the UV light curve seen around a couple days prior to merger, at the vertical dashed line corresponding to the decoupling timescale in Fig. 15.

Years before merger, the majority of the overall accretion power is released as X-rays, from the small secondary disk. However as the inspiral proceeds, the outer disk reaches deeper into the gravitational potential of the primary, glowing brighter in the UV, while the secondary is gradually starved, and gets dimmer in the X-rays. The outer disk follows the inspiraling secondary black hole and as it does so, the inner edge of the outer disk increases in speed and heats up the gas leading to a brightening effect. The UV brightening peaks at the time when the disk viscously decouples from the binary as seen in Fig. 14 at $t_{\text{minus}} \simeq 1$ day. For the fiducial disk-binary model, the

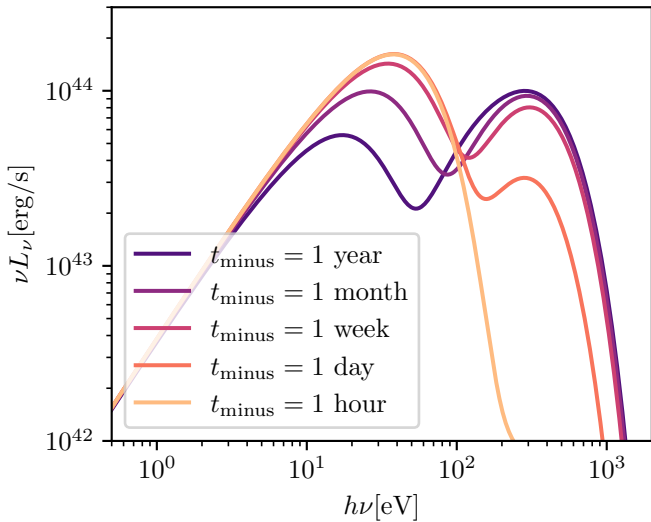


Figure 14. Evolution of the total spectral energy distribution of thermal emission produced by the fiducial system from 1 year before merger (purple) to 1 hour before merger (yellow). The model assumes that the accretion flow can be characterized as a steady state α -disk, with radial temperature profile given by Eqn. 3.

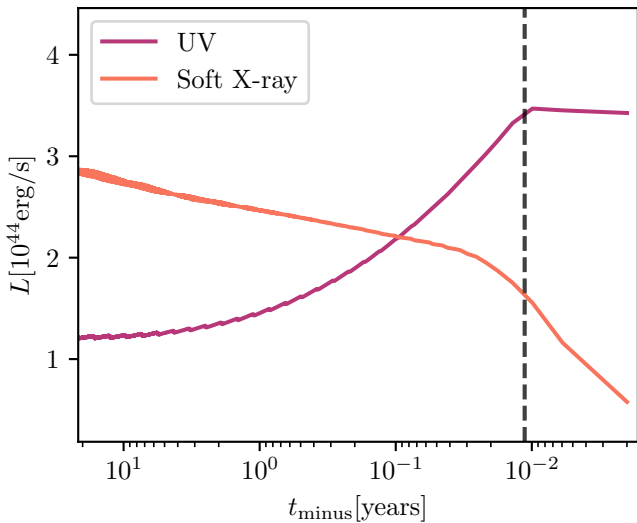


Figure 15. Light curves of the UV (3.3 – 100 eV) and X-ray (0.25 – 5 keV) emission obtained by integrating the luminosity found in Fig. 1 over each energy band at each time. Light curves shown for the fiducial binary where mass ratio is $q = 0.01$ and orbital Mach number is $\mathcal{M} = 10$. Dashed line corresponds to the viscous decoupling timescale in Eqn. 7.

X-ray emission is surpassed by the UV emission on the order of one month before the merger. At the same time as the peaking of the UV emission, the X-ray emission from the secondary disk decays because of the fast reduction in the rate of mass supplied to the secondary very late in the inspiral (Krauth et al. 2023b). This is also evident in the measured accretion rates in Fig. 5.

We do not show the post-merger EM signatures associated with the remnant fueling curves presented in Sec. 4.3, because the disk is far from being viscously relaxed while the accretion rate recovers to \dot{M}_0 . Analytic estimates for this phase are presented in Milosavljević & Phinney (2005); Schnittman & Krolik (2008). We also do not

show the orbital period variations in the light curves or spectrum, as these cannot generally be captured in the three-disk model. Spectral evolution on the time scale of individual binary orbits requires a self-consistent thermodynamic treatment and will be presented in a future work (see Sec. 6.2).

5.2 Prospects for EM Detections

Here we consider how our results might influence proposed strategies to discover the EM counterparts of *LISA* GW detections. As discussed in the introduction, EM counterparts from *LISA* sources will likely be needed to confidently identify the host galaxies of MBHB inspirals.

Our results indicate that in the years before a merger, accreting unequal-mass black hole binaries get brighter in the UV, and dimmer in the X-ray. They also exhibit an abrupt disappearance in X-rays in the final hours to days before the merger. We further predict that variations at the orbital period should be discernible at the tens-of-percent level, resulting from orbital-period modulations of the accretion onto the secondary. Observatories carrying out time domain surveys, or space observatories capable of slewing in response to a GW trigger, could thus be instrumental in EM counterpart identification. We discuss below the relevance of these predictions to the current and upcoming observatories *Roman*, *Vera Rubin*, *UVEX*, *Athena* and *eROSITA*.

5.2.1 Nancy Grace Roman

The *Nancy Grace Roman Space Telescope* is a wide-field optical to near-infrared space telescope, anticipated to begin operation in 2027. *Roman* could potentially detect periodicity in an accreting MBHB, corresponding to the quasi-periodic variability of the mass accretion rates shown in the insets of Figs. 8 and 9. Such periodicity detections by *Roman* could become extremely valuable if the system is 10 – 20 years away from merging, because the merger might then take place during the *LISA* period of operation (Haiman et al. 2023). As discussed in Sec. 2.1, a $10^7 M_\odot$ binary that is 50 years away from merging has a rest-frame orbital period of 1.8 days. At $z \sim 1-2$ this corresponds to multi-day periodicity, comparable to the anticipated ~ 5 day cadence planned for the *Roman* high latitude time domain survey. Our calculations in Sec. 4.4 only predict the periodic variations of the mass accretion rates, so follow-up calculations will be needed to predict the level of periodicity expected in the IR through optical wavelengths, where *Roman* is sensitive. This is an intended area of future work, see Sec. 6.2.

5.2.2 Vera Rubin

The Legacy Survey of Space and Time (*LSST*) will be carried out over at least the first 10 years of the operation of *Vera Rubin*, which is now aimed to begin operation in late 2025. *LSST* will observe nearly half the sky, $18,000 \text{ deg}^2$, and will detect up to 10^6 galaxies per square degree, observing quasars with a cadence of once per day (Xin & Haiman 2021). *Vera Rubin's LSST* camera will be sensitive at near-UV through near-IR wavelengths, so the steady UV brightening we are predicting to accompany a *LISA* inspiral could be evident in *LSST* archival data over the 10 years prior to a GW detection by *LISA*. Similar to *Roman*, *LSST* could potentially detect the modulating brightness of an accreting MBHB, corresponding to the quasi-periodic variability of the mass accretion rates. See Xin & Haiman (2024) for a detailed analysis of using archival *LSST* data to search for *LISA* EM counterparts and the feasibility of doing so.

5.2.3 UVEX

The UltraViolet EXplorer telescope, *UVEX*, is a recently selected NASA Explorer mission that will launch around 2030. *UVEX* will have highly sensitive far-UV and near-UV wide-field imagers (WFI's; Kulkarni et al. 2021). *UVEX* will supplement *LSST* and *Roman* by providing an all-sky data set in the far-UV energy range. Although a main objective for *UVEX* is to observe the aftermaths of binary neutron star mergers, our results suggest that *UVEX* could also be suitable for detecting the UV precursors of *LISA* inspirals. Due to the extended nature of the predicted UV brightening, such precursors could be evident in archival data and could thus aid in host galaxy identification, even if the *UVEX* mission lifetime does not overlap with *LISA*'s. The utility of *UVEX* in finding the predicted gradual UV brightening of a *LISA* inspiral is increased if the all-sky survey will repeatedly image individual sky patches throughout the mission lifetime.

5.2.4 Athena

The *Athena* X-ray telescope will be operating over 4 years in the 2030s and will observe hundreds of X-ray sources, potentially including the inspiral and merger of MBHB's. It is also possible that *Athena* could operate simultaneously with *LISA*. *Athena* will perform around 300 pointed observations of targets each year with a duration of $10^3 - 10^6$ seconds. For the fiducial binary considered in this paper, about 70% (46%) of the events at redshift $z = 0.3$ ($z = 1$) will have *LISA* localization ($1 - 10 \text{ deg}^2$) smaller than the *Athena* Wide Field Imager (WFI) field of view (0.4 deg^2 ; Piro et al. 2023). As *LISA* observes an inspiral, the localization improves, and we suggest that once the localization is comparable to or smaller than the WFI field of view, *Athena* should then have time to slew (which can take between 2 – 4 hours) to the error in time to observe the X-ray disappearance before merger and identify the host galaxy (Nandra et al. 2013). A similar strategy for *Athena* is also discussed in Krauth et al. (2023b).

5.2.5 eROSITA

eROSITA is a current X-ray detector on the Spektr-RG space observatory that was launched in 2019 and has since been taking an all-sky, high cadence survey at high latitude of the soft (0.5 – 2 keV) and hard X-rays (2 – 10 keV; Merloni et al. 2012). There is a chance that *eROSITA*'s operation timeline could overlap with *LISA*'s, but in general *eROSITA* could provide a reference sky template to aid in host galaxy characterization. For example, once *LISA* detects the GW signatures from a merging MBHB and *Athena* aids in identifying the host galaxy, it could then be possible that *eROSITA* had previously characterized the X-ray emission from the same galaxy, some 10–20 years before merger. Comparisons can be made between *Athena* and *eROSITA* data of the same galaxy, to determine the long term X-ray variability. Thus, using *Athena* and *eROSITA* to jointly search for the X-ray signatures of black hole binary inspirals could increase the likelihood of multi-messenger detections.

6 SUMMARY

6.1 Main Results

Using analytic estimates and high-resolution grid-based hydrodynamics simulations, we have explored the gas dynamics and EM signatures of accreting binary black holes with significantly unequal masses, $q = 10^{-3} - 10^{-1}$ and $M \sim 10^7 M_\odot$, over decade-like

timescales before a merger. Our aim is to help enable EM counterpart detection, and host galaxy identification, of binary black hole inspirals observed by *LISA*. Our main results are summarized here:

(i) The viscous decoupling time is generally on the order of $\tau_{\text{dec}} \sim$ days for $\sim 10^7 M_\odot$ binaries. One might reasonably expect the binary accretion rate \dot{M} to remain steady until $\sim \tau_{\text{dec}}$ before merger, however our simulations show significant reductions in \dot{M} over decade-like time scales, $10^3 \tau_{\text{dec}}$. We attribute this effect to the decrease of angular momentum current through the disk, accompanying the binary contraction. A model of this process is the subject of a forthcoming work.

(ii) Low mass ratio binaries show accretion rate variability at the orbital period, at the level of around 10%. Stochastic variability is reduced throughout the inspiral when the mass ratio is smaller than the threshold $q \sim 0.04$ found by D'Orazio et al. (2016). The secondary generally consumes most of the mass coming to the binary (preferential accretion effect). Both components are gradually starved of mass supply as the inspiral progresses, but the secondary starves more slowly than the primary.

(iii) EM flares produced by tidal squeezing of the inner disk (snowplow effect) are not expected. This is based on dynamical considerations and confirmed in the simulations; the tidal torque becomes too weak years before merger to reduce the orbits of inner disk gas parcels faster than \dot{a}_{gw} . Instead the inner disk gas accretes to the secondary during the inspiral, leading to the observed slower starvation of the secondary.

(iv) We developed a toy-model for the quasi-thermal emission spectrum of the accretion flow surrounding a low mass ratio binary black hole, based on the assumption that the outer, inner, and secondary disks are viscously relaxed. The simple model predicts an emission spectrum with peaks in the UV and X-ray, reflecting the characteristic temperatures of the outer and circum-secondary disks respectively. Those disks out-shine the inner (primary) disk because of the preferential accretion effect.

(v) Together with the mass accretion rates measured in the simulations, the toy model predicts a decade-like gradual brightening in the UV, and dimming in the X-ray, followed by an abrupt disappearance of the X-rays around time $\tau_{\text{dec}} \sim$ days before the merger (analogous to Krauth et al. 2023b), and finally year-like gradual X-ray re-brightening associated with fueling of the remnant black hole. The long-term pre-merger UV brightening is the result of the increasing peak temperature of the outer disk, as it extends deeper into the potential well of the primary throughout the inspiral.

6.2 Caveats and Future Work

Our simulations are based on two-dimensional (vertically averaged) solutions of the Navier-Stokes equations in the locally isothermal approximation; the effects of shock heating, radiation, magnetic fields, general relativity, and out-of-plane gas flows including winds and jets, are all neglected. Other groups are actively exploring these, especially in the context of near-equal mass ratio binaries in the final tens of orbits before a merger (see references given in the introduction). The simplified simulations presented here were necessary to study the long-term dynamics and EM signatures, and may be accurate enough to help identify host galaxies of *LISA* events.

In a future work, we will present simulations of unequal-mass inspirals with a more realistic thermodynamics treatment, to properly account for shock heating, as done with the *Sailfish* code in Westernacher-Schneider et al. (2022, 2024); Krauth et al. (2023a,b); DeLaurentiis et al. (2024). In the context of near-equal mass bina-

ries, shock-heating does significantly alter the profile of disk surface temperature (e.g. Farris et al. 2015). However when the mass ratio is small, we expect less of the gas orbital energy to be dissipated in strong shocks, so the result might be not very different from the spectrum toy model we presented here.

We do not expect general relativistic effects to significantly alter the long-term brightness and color changes of a binary-host quasar in the years before a merger, because the long-term changes are driven by large-scale viscous relaxation of the disk far from the gravitational radii of either black hole. Note however, that relativistic apsidal precession can modulate the amplitude of periodicity in the gas-driven evolutionary phase (DeLaurentiis et al. 2024). Accounting for magnetic fields and radiation could change some of our predictions, especially in a regime where the mass flow to the binary is comparable to the Eddington rate of the primary. In such cases, preferential accretion implies the secondary tries to accrete much faster than its own Eddington rate, and that radiation-driven outflows could significantly change the global mass currents in the system.

ACKNOWLEDGEMENTS

M. Clyburn acknowledges support from the NASA Future Investigators Program (FINESST) through Award No. 80-NSSC-23K1443. J. Zrake acknowledges support from the *LISA* Preperatory Science Program (LPS) through NASA Award No. 80-NSSC-24K0440. J. Zrake also acknowledges valuable discussion with Alex Dittmann, Sterl Phinney, Julian Krolik, Elena Rossi, and Zoltan Haiman, some of which took place at the 2022 binary accretion workshop hosted by the Kavli Institute for Theoretical Physics (KITP); this research was supported in part by grant NSF PHY-1748958 to KITP. All simulations were performed on Clemson University’s Palmetto cluster.

DATA AVAILABILITY

The data underlying this article will be shared on reasonable request to the corresponding author.

REFERENCES

Amaro-Seoane P., et al., 2023, *Living Reviews in Relativity*, 26, 2
 Arca Sedda M., Amaro Seoane P., Chen X., 2021, *A&A*, 652, A54
 Armitage P. J., Natarajan P., 2002, *ApJ*, 567, L9
 Armitage P. J., Natarajan P., 2005, *ApJ*, 634, 921
 Avara M. J., Krolik J. H., Campanelli M., Noble S. C., Bowen D., Ryu T., 2023, *arXiv e-prints*, p. arXiv:2305.18538
 Baibhav V., Berti E., Cardoso V., 2020, *Phys. Rev. D*, 101, 084053
 Barnes J. E., Hernquist L., 1996, *The Astrophysical Journal*, 471, 115
 Baruteau C., Ramirez-Ruiz E., Masset F., 2012, *MNRAS*, 423, L65
 Begelman M. C., Blandford R. D., Rees M. J., 1980, *Nature*, 287, 307
 Bellovary J., et al., 2019, *BAAS*, 51, 175
 Bortolas E., Franchini A., Bonetti M., Sesana A., 2021, *ApJ*, 918, L15
 Bowen D. B., Mewes V., Campanelli M., Noble S. C., Krolik J. H., Zilhão M., 2018, *The Astrophysical Journal Letters*, 853, L17
 Bowen D. B., Mewes V., Noble S. C., Avara M., Campanelli M., Krolik J. H., 2019, *The Astrophysical Journal*, 879, 76
 Brandt W. N., et al., 2009, in , LSST Science Book. LSST Corporation, Chapt. 10
 Chang P., Strubbe L. E., Menou K., Quataert E., 2010, *MNRAS*, 407, 2007
 Cocchiararo F., Franchini A., Lupi A., Sesana A., 2024, *arXiv e-prints*, p. arXiv:2402.05175
 Combi L., Armengol F. G. L., Campanelli M., Ireland B., Noble S. C., Nakano H., Bowen D., 2021, *Phys. Rev. D*, 104, 044041

Cuadra J., Armitage P. J., Alexander R. D., Begelman M. C., 2009, *MNRAS*, 393, 1423
 D’Orazio D. J., Duffell P. C., 2021, *ApJ*, 914, L21
 D’Orazio D. J., Haiman Z., Duffell P., MacFadyen A., Farris B., 2016, *MNRAS*, 459, 2379
 DeLaurentiis S., Haiman Z., Westernacher-Schneider J. R., Krauth L. M., Davelaar J., Zrake J., MacFadyen A., 2024, *Relativistic Binary Precession: Impact on Eccentric Binary Accretion and Multi-Messenger Astronomy* (arXiv:2405.07897)
 Derdzinski A. M., D’Orazio D., Duffell P., Haiman Z., MacFadyen A., 2019, *MNRAS*, 486, 2754
 Derdzinski A., D’Orazio D., Duffell P., Haiman Z., MacFadyen A., 2021, *MNRAS*, 501, 3540
 Dittmann A. J., Ryan G., Miller M. C., 2023, *ApJ*, 949, L30
 Duffell P. C., Haiman Z., MacFadyen A. I., D’Orazio D. J., Farris B. D., 2014, *ApJ*, 792, L10
 Duffell P. C., D’Orazio D., Derdzinski A., Haiman Z., MacFadyen A., Rosen A. L., Zrake J., 2020, *ApJ*, 901, 25
 Duffell P. C., et al., 2024, *arXiv e-prints*, p. arXiv:2402.13039
 Escala A., Larson R. B., Coppi P. S., Mardones D., 2005, *ApJ*, 630, 152
 Farris B. D., Liu Y. T., Shapiro S. L., 2010, *Phys. Rev. D*, 81, 084008
 Farris B. D., Liu Y. T., Shapiro S. L., 2011, *Phys. Rev. D*, 84, 024024
 Farris B. D., Gold R., Paschalidis V., Etienne Z. B., Shapiro S. L., 2012, *Phys. Rev. Lett.*, 109, 221102
 Farris B. D., Duffell P., MacFadyen A. I., Haiman Z., 2014, *ApJ*, 783, 134
 Farris B. D., Duffell P., MacFadyen A. I., Haiman Z., 2015, *MNRAS*, 447, L80
 Franchini A., Sesana A., Dotti M., 2021, *MNRAS*, 507, 1458
 Franchini A., Bonetti M., Lupi A., Sesana A., 2024, *arXiv e-prints*, p. arXiv:2401.10331
 Fung J., Shi J.-M., Chiang E., 2014, *ApJ*, 782, 88
 Garg M., Tiwari S., Derdzinski A., Baker J. G., Marsat S., Mayer L., 2024, *MNRAS*, 528, 4176
 Goldreich P., Tremaine S., 1980, *ApJ*, 241, 425
 Gutiérrez E. M., Combi L., Noble S. C., Campanelli M., Krolik J. H., López Armengol F., García F., 2022, *ApJ*, 928, 137
 Haiman Z., et al., 2023, *arXiv e-prints*, p. arXiv:2306.14990
 Hughes S. A., 2002, *MNRAS*, 331, 805
 Izquierdo-Villalba D., Sesana A., Bonoli S., Colpi M., 2022, *MNRAS*, 509, 3488
 Kley W., Dirksen G., 2006, *A&A*, 447, 369
 Krauth L., Davelaar J., Haiman Z., Westernacher-Schneider J. R., Zrake J., MacFadyen A., 2023a, *arXiv e-prints*, p. arXiv:2310.19766
 Krauth L. M., Davelaar J., Haiman Z., Westernacher-Schneider J. R., Zrake J., MacFadyen A., 2023b, *MNRAS*, 526, 5441
 Kulkarni S. R., et al., 2021, *arXiv e-prints*, p. arXiv:2111.15608
 Lin D. N. C., Papaloizou J., 1986, *ApJ*, 309, 846
 Liu F. K., Wu X.-B., Cao S. L., 2003, *MNRAS*, 340, 411
 Lodato G., Nayakshin S., King A. R., Pringle J. E., 2009, *MNRAS*, 398, 1392
 Lubow S. H., Seibert M., Artymowicz P., 1999, *ApJ*, 526, 1001
 Mangiagli A., et al., 2020, *Phys. Rev. D*, 102, 084056
 Merloni A., et al., 2012, *arXiv e-prints*, p. arXiv:1209.3114
 Miller M. C., 2009, *Classical and Quantum Gravity*, 26, 094031
 Milosavljević M., Phinney E. S., 2005, *ApJ*, 622, L93
 Moody M. S. L., Shi J.-M., Stone J. M., 2019, *ApJ*, 875, 66
 Muñoz D. J., Lai D., Kratter K., Miranda R., 2020, *ApJ*, 889, 114
 Nandra K., et al., 2013, *arXiv e-prints*, p. arXiv:1306.2307
 Noble S. C., Mundim B. C., Nakano H., Krolik J. H., Campanelli M., Zlochower Y., Yunes N., 2012, *ApJ*, 755, 51
 Penzlin A. B. T., Kley W., Audiffren H., Schäfer C. M., 2022, *A&A*, 660, A101
 Pereira F. A. C., Lodato G., Rodrigues I., Alves M. E. S., Price D. J., 2019, *MNRAS*, 484, 31
 Peters P. C., 1964, *Physical Review*, 136, 1224
 Piro L., et al., 2023, *MNRAS*, 521, 2577
 Pitte C., Baghi Q., Marsat S., Besançon M., Petiteau A., 2023, *Phys. Rev. D*, 108, 044053
 Pringle J. E., 1981, *ARA&A*, 19, 137

- Rafikov R. R., 2016, *The Astrophysical Journal*, 827, 111
- Roedig C., Dotti M., Sesana A., Cuadra J., Colpi M., 2011, *MNRAS*, 415, 3033
- Ruiz M., Tsokaros A., Shapiro S. L., 2023, *arXiv e-prints*, p. [arXiv:2302.09083](https://arxiv.org/abs/2302.09083)
- Schnittman J. D., Krolik J. H., 2008, *ApJ*, 684, 835
- Schutz B. F., 1986, *Nature*, 323, 310
- Sesana A., 2021, *Frontiers in Astronomy and Space Sciences*, 8, 7
- Sesana A., Roedig C., Reynolds M. T., Dotti M., 2012, *MNRAS*, 420, 860
- Shakura N. I., Sunyaev R. A., 1973, *A&A*, 24, 337
- Shi J.-M., Krolik J. H., 2015, *The Astrophysical Journal*, 807, 131
- Siwek M. S., Kelley L. Z., Hernquist L., 2020, *MNRAS*, 498, 537
- Siwek M., Weinberger R., Muñoz D. J., Hernquist L., 2023a, *MNRAS*, 518, 5059
- Siwek M., Weinberger R., Hernquist L., 2023b, *MNRAS*, 522, 2707
- Tang Y., Haiman Z., MacFadyen A., 2018, *MNRAS*, 476, 2249
- Tiede C., D’Orazio D. J., 2024, *MNRAS*, 527, 6021
- Tiede C., Zrake J., MacFadyen A., Haiman Z., 2020, *ApJ*, 900, 43
- Tiede C., Zrake J., MacFadyen A., Haiman Z., 2022, *ApJ*, 932, 24
- Tiede C., D’Orazio D. J., Zwick L., Duffell P. C., 2024, *ApJ*, 964, 46
- Trias M., Sintes A. M., 2008, *Classical and Quantum Gravity*, 25, 184032
- Valli R., et al., 2024, *arXiv e-prints*, p. [arXiv:2401.17355](https://arxiv.org/abs/2401.17355)
- Westernacher-Schneider J. R., Zrake J., MacFadyen A., Haiman Z., 2022, *Phys. Rev. D*, 106, 103010
- Westernacher-Schneider J. R., Zrake J., MacFadyen A., Haiman Z., 2024, *ApJ*, 962, 76
- Xin C., Haiman Z., 2021, *MNRAS*, 506, 2408
- Xin C., Haiman Z., 2024, *arXiv e-prints*, p. [arXiv:2403.18751](https://arxiv.org/abs/2403.18751)
- Young M. D., Clarke C. J., 2015, *MNRAS*, 452, 3085
- Yunes N., Kocsis B., Loeb A., Haiman Z., 2011, *Phys. Rev. Lett.*, 107, 171103
- Zrake J., Tiede C., MacFadyen A., Haiman Z., 2021, *ApJ*, 909, L13

This paper has been typeset from a $\text{\TeX}/\text{\LaTeX}$ file prepared by the author.